Chemical Engineering Journal 158 (2010) 362–367

Contents lists available at ScienceDirect

Chemical Engineering Journal

journal homepage: www.elsevier.com/locate/cej

Particle dynamics simulation of nanoparticle formation in a flame reactor using a polydispersed submicron-sized solid precursor

W. Widiyastuti[a], Darmawan Hidayat[b], Agus Purwanto[c], Ferry Iskandar[b], Kikuo Okuyama[b,*]

[a] Department of Chemical Engineering, Faculty of Industrial Technology, Institut Teknologi Sepuluh Nopember (ITS), Kampus ITS Keputih-Sukolilo, Surabaya 60111, Indonesia
[b] Department of Chemical Engineering, Graduate School of Engineering, Hiroshima University, 1-4-1 Kagamiyama, Higashi-Hiroshima 739-8527, Japan
[c] Department of Chemical Engineering, Faculty of Engineering, Sebelas Maret University, Jl. Ir. Sutami 36 A, Surakarta, Central Java 57126, Indonesia

ARTICLE INFO

Article history:
Received 6 November 2009
Received in revised form 30 January 2010
Accepted 4 February 2010

Keywords:
Tungsten oxide
Evaporation
A gas-phase route
Non-spherical particles

ABSTRACT

Formation of nanoparticles from polydispersed, non-spherical submicron-sized particles via a gas-phase route in a flame reactor was investigated using tungsten oxide particles as a model material. Nanoparticles were formed by the evaporation of non-spherical powder, followed by nucleation, coagulation and surface condensation. The effects of both the flame temperature profile and the carrier gas flow rate on particles formation were studied numerically, and the results were validated by experimental data. The simulation was initiated by the use of computational fluid dynamics (CFD) to obtain the temperature distribution in the flame reactor. Then, evaporation of the feed material was modeled, taking into account both the polydispersity and the shape of the non-spherical particles. A nodal method was selected to solve the general dynamics equation (GDE), which included nucleation, coagulation, and surface condensation terms, for the prediction of particle dynamics. Results of the simulation were consistent with the experimental data, indicating that the selected model adequately predicts the final particle size distribution.

1. Introduction

Nanoparticles that range in size from tens to hundreds of nanometers are the focus of current research because their chemical and physical behaviors are remarkably different from those of the bulk material [1,2]. Nanoparticles exhibit superior optical, electronic and luminescence properties compared with materials of larger grain sizes. Nanoparticles can be formed using aerosol process that has advantages over liquid processes: high purity, continue process, and a short residence time [1,3]. The use of flame synthesis in aerosol processes for the generation of nanoparticles from feeding material in the gas-, liquid- or solid-phase is becoming increasingly popular. The use of monodispersed and spherical silica powder as an ideal feed material for flame synthesis was introduced by our group, and particle formation using this material has been evaluated both experimentally and theoretically [4]. The advantages of solid-fed flame synthesis for the generation of nanoparticles include a one-step process and an inexpensive, easy-to-handle bulk material as the feed material.

In general, polydispersed and irregularly shaped powder is inexpensive and easily obtained, which enhances its potential for use as a feed material. One candidate model material is tungsten oxide because polydispersed and irregularly shaped micro-submicrometer tungsten oxide powder is commercially available. A solid-fed flame process that can generate highly crystalline tungsten oxide nanoparticles from the bulk particles with controllable size, high adsorption and relatively low production costs was studied experimentally in our previous investigation [5]. Tungsten oxide nanoparticles can be applied to the development of future technologies, such as photocatalysis, solar energy devices, color memory devices, and gas sensors [6–9]. Therefore, quantitative studies of the controllability of nanoparticle formation by solid-fed flame synthesis are necessary to determine the optimal design and operation of flame reactors for the generation of particles with a predictable particle size distribution. Current investigations of solid-fed flame synthesis are limited to monodispersed and spherical bulk materials [4]. Quantitative study of nanoparticle formation using solid-fed flame synthesis starting with polydispersed and irregularly shaped powder as the feed material is important to better understand the process.

In solid-fed flame synthesis modeling, there are two routes: solid evaporation for vapor generation and gas-to-particle conversion for generation of nanoparticles via vapor nucleation, coagulation, and surface condensation mechanisms [4]. Evaporation modeling was applied to calculate the monomer concentration in the continuous phase that resulted from a solid evaporation

---

* Corresponding author. Tel.: +81 82 424 7716; fax: +81 82 424 5494.
E-mail address: okuyama@hiroshima-u.ac.jp (K. Okuyama).

1385-8947/$ – see front matter © 2010 Elsevier B.V. All rights reserved.
doi:10.1016/j.cej.2010.02.008

Nomenclature

D_v	vapor diffusion coefficient ($m^2\,s^{-1}$)
$N(1)$	tungsten oxide vapor number concentration (m^{-3})
$N(k)$	number concentration of tungsten oxide particles at the kth node (m^{-3})
$R_{i,r}$	the net rate of production of species i due to reaction r ($kg\,m^{-3}\,s^{-1}$)
T	temperature (K)
$d_{p,i}$	particle diameter of size class i (m)
k_B	Boltzmann constant ($J\,K^{-1}$)
m_1	mass of a tungsten oxide molecule (kg)
n_i	initial particle number concentration of size class i (m^{-3})
n_s	saturated tungsten oxide vapor concentration, molecules (m^{-3})
p_s	saturated pressure ($N\,m^{-2}$)
s_1	surface of a tungsten oxide molecule (m^2)
t	time (s)

Greek letters

ρ_p	particle density ($kg\,m^{-3}$)
ϕ_S	sphericity shape factor (dimensionless)

process in the high-temperature region near the burner surface of the flame reactor. When the flame temperature decreased, supersaturation occurred, leading to nanoparticle formation by nucleation, coagulation and condensation. Gas-to-particle conversion itself has been reviewed extensively, both theoretically and experimentally [2,10]. Most numerical models used to describe particle formation via aerosol routes following gas-to-particle conversion are based on the general dynamic equation (GDE). These models include sectional, moment, discrete-sectional, nodal, and discrete-nodal point methods [11–15]. The GDE solution can also be modified or extended.

This paper introduces a modification of our previous model of nanoparticle formation via solid-fed flame synthesis using polydispersed and non-spherical particles as a starting material. The use of tungsten oxide powder, rather than silica, as the starting material proves that the model can be applied to various materials, depending on their physical and chemical characteristics. The effects of both fuel flow rate and carrier gas flow rate on the final particles were investigated numerically, and the results were validated by experimental data.

2. Experimental

The experimental system, which consisted of an aerosol generator, a flame burner and a bag filter for particle collection, is shown in Fig. 1a. The flame reactor was also equipped with a Pyrex glass cylinder that was 96 mm in diameter and 1 m in height. Methane and oxygen were selected as fuel and oxidizer, respectively, with volume ratio 1:2.5 to assure combustion completely. Solid precursor with feed rate of 1140 mg/h was carried by oxygen as a carrier gas. The system is described in detail in our previous paper [4]. The morphologies of the initial and generated particles were examined using a field emission-scanning electron microscope (FE-SEM, S-5000, Hitachi Corp., Tokyo, Japan). Geometric mean particle size, d_g, geometric standard deviation, σ_g, and sphericity shape factor, ϕ_s, were determined from the FE-SEM images of at least 400 particles. The particle size distribution of the initial tungsten oxide feed material is depicted in Fig. 1b and d_g and σ_g were 674 nm and 1.45, respectively. The initial tungsten oxide particles were non-spherical as shown in the FE-SEM image in Fig. 1c. The sphericity shape factor of the feed particles was determined using an image analyzer (ImageJ, free software). The sphericity shape factor, ϕ_s, of particles is defined as the ratio of the surface area of a sphere with the same volume as the particle to the actual surface area of the particle, $\phi_S = d_p^2/S_p$, where S_p is the actual surface of the particle and d_p is the diameter (equivalent diameter) of the sphere having the same volume as the particle [16]. The sphericity shape factor is also defined as the ratio of the ($4\pi A$) to the (P^2), where A is the

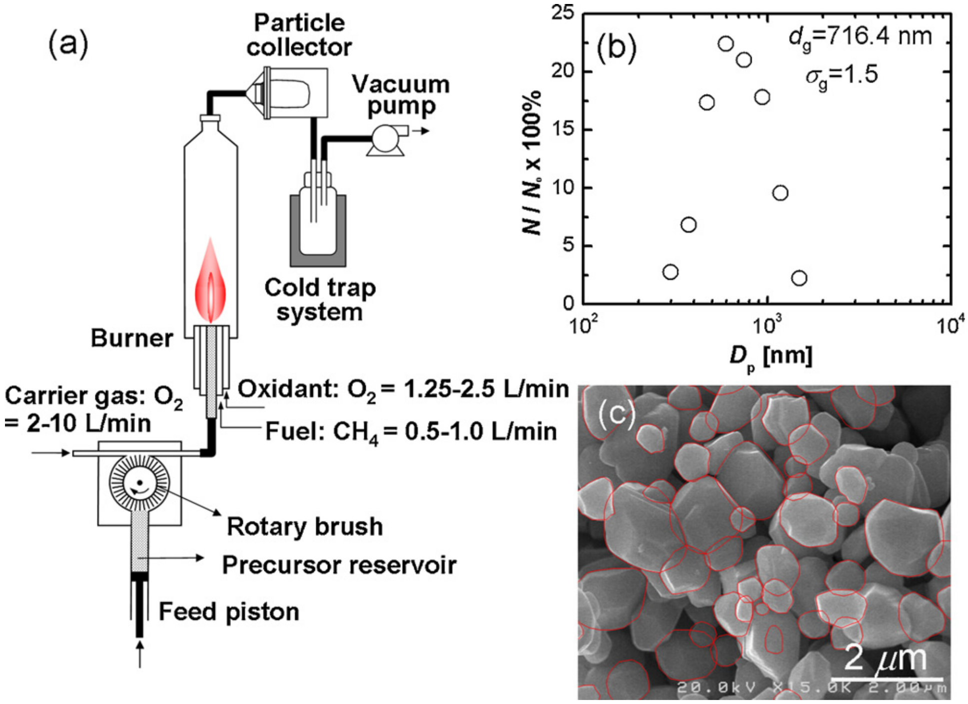

Fig. 1. (a) Experimental set-up, (b) size distribution of the initial tungsten oxide particles, and (c) FE-SEM image of the initial tungsten oxide particles.

area and P is the perimeter of the particles, which is easier to determine than sphericity estimated from the particle image [17]. The sphericity shape factor of the feed particles was 0.90.

3. Numerical method

The simulation was begun by obtaining the temperature profile and velocity distribution in the domain system of the flame reactor using a commercial CFD code, FLUENT 6.3 (Fluent Asia Pacific, Tokyo, Japan). The details of the CFD method used for flame combustion modeling and its validation are described in our previous investigation [4].

To model the size changes in feed particle due to solid evaporation, both the polydispersity and sphericity shape factor of the feed particles, which was disregarded in our earlier study [4], were considered. To model the evaporation rate of evaporation of polydispersed feed particles, the size distribution was divided into j size fractions, as in our previous model of droplets containing the precursor solution [18]. Therefore, there were j simultaneous equations for the rate of tungsten oxide particle evaporation as follows:

$$\frac{\mathrm{d}d_{\mathrm{p},i}}{\mathrm{d}t} = \frac{4D_{\mathrm{v}}m_1}{\rho_{\mathrm{p}}d_{\mathrm{p},i}}(N(1) - n_{\mathrm{s}})\phi_{\mathrm{S}}, \quad i = 1, 2, \ldots, j; \;\; j = 8 \tag{1}$$

The change in tungsten oxide vapor in the surrounding gas is given by the following equation:

$$\frac{\mathrm{d}N(1)}{\mathrm{d}t} = -2\pi D_{\mathrm{v}}\sum_{i=1}^{i} d_{\mathrm{p},i}n_i(N(1) - n_{\mathrm{s}})\phi_{\mathrm{S}}, \quad i = 1, 2, \ldots, j; \;\; j = 8 \tag{2}$$

Both equations assumed that the saturation ratio was less than or equal to 1 and that $d_{\mathrm{p},i}$ was greater than or equal to zero. ϕ_{S} is the sphericity or shape factor that should be considered for improvement of the results of arbitrary bodies, $U_{\text{arbitrary body}} = \phi_{\mathrm{S}}\, U_{\text{sphere}}$, where U is an arbitrary quantity of interest [19].

The saturation concentration, n_{s}, was obtained using the following equation:

$$n_{\mathrm{s}} = \frac{p_{\mathrm{s}}}{k_{\mathrm{B}}T} \tag{3}$$

where p_{s} is the vapor pressure of tungsten oxide, which was obtained from tungsten oxide vapor pressure data [20]. Correlation of the data resulted in the following equation:

$$p_{\mathrm{s}} = \exp\left(45.46 - \frac{54070.6}{T}\right) \tag{4}$$

Surface tension data are assumed independent of temperature, according to Vladuta et al. [21] to obtain vapor diffusivity, D_{v}, a correlation based on physical–chemical data taken from Poling et al. [22] was used.

Due to a non-homogenous temperature distribution in the flame reactor, supersaturation was achieved in the cooling region of the flame reactor. The tungsten oxide vapors generated the smallest particles, which are called clusters, by homogenous nucleation. Then, the clusters increased in size via coagulation and surface condensation. For simultaneous nucleation, coagulation and condensation, the following general dynamics equation (GDE) was solved [4,15]:

$$\frac{\mathrm{d}N(k)}{\mathrm{d}t} = \left.\frac{\mathrm{d}N(k)}{\mathrm{d}t}\right|_{\text{nucl}} + \left.\frac{\mathrm{d}N(k)}{\mathrm{d}t}\right|_{\text{coag}} + \left.\frac{\mathrm{d}N(k)}{\mathrm{d}t}\right|_{\text{evap/cond}} \tag{5}$$

where $N(k)$ is the number concentration of the particles at node k. Details of the nucleation, coagulation, and surface condensation terms are described in previous papers [4,15]. These equations were solved using a nodal method, in which the particle size distribution was discretizing in size or volume space and the solution to the population balance equation was determined for each section. In this simulation, particles were assumed coalescence fully to form spherical particles.

4. Results and discussion

4.1. Temperature distribution

The temperature distributions along the center and x–y planar crossing the center of the flame reactor under various conditions obtained from the CFD simulation are shown in Fig. 2a and b. The temperature increased in the region near the burner surface and continued to increase up to the maximum temperature at a certain position and then decreased up to the end of the flame reactor. The maximum temperature increased as the methane flow rate was increased. At a constant carrier gas flow rate of 10 L/min, the maximum temperatures at locations within 10 cm of the burner surface were approximately 1500, 1300, and 1100 °C at methane flow rates of 1.0, 0.8, and 0.5 L/min, respectively. At distances greater than 10 cm, the temperature decreased steeply. For methane flow rates of 1.0, 0.8, and 0.5 L/min, the total residence times were 7.2, 7.9, and 8.7 s, respectively. On the other hand, at a methane flow rate of 1 L/min and a lower carrier gas flow rate of 2 L/min, the temperature and the residence time were 2500 °C and 10.2 s, respectively. Decreasing the carrier gas flow rate increased both

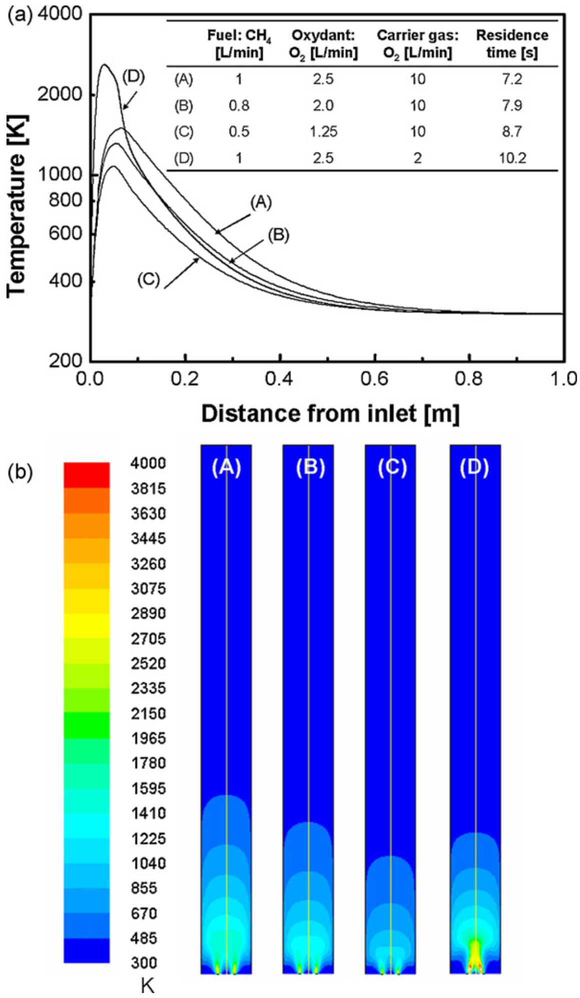

Fig. 2. Temperature distributions (a) along the center of and (b) x–y planar crossing the center of the flame reactor under various operating conditions.

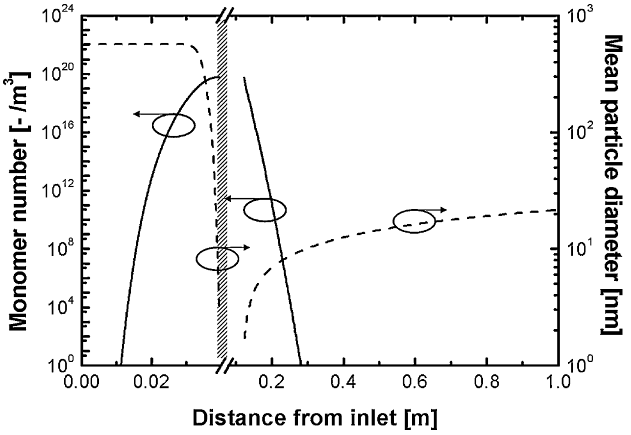

Fig. 3. Change in the monomer number concentration and average particle size along the furnace length. Operating condition: methane (fuel) flow rate of 1 L/min and an oxygen (carrier gas) flow rate of 10 L/min.

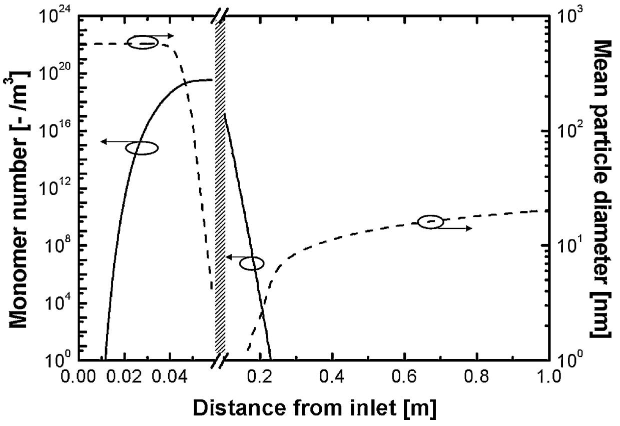

Fig. 5. Change in the monomer number concentration and average particle size along the furnace length. Operating condition: methane (fuel) flow rate of 0.8 L/min and an oxygen (carrier gas) of 10 L/min.

flame temperature and the total residence time. Similar trends were also obtained in our previous simulation results [4]. The effects of fuel flow rate and carrier gas flow rate are summarized in the inset of Fig. 2.

4.2. Effect of flow rate of methane as a fuel source

To investigate the effect of the methane flow rate on the synthesized particles, we selected flow rates of 1.0, 0.8, and 0.5 L/min, i.e., conditions (A), (B), and (C) in Fig. 2, respectively, at a constant carrier gas flow rate of 10 L/min as indicated by the table in the inset of Fig. 2. For (A), changes in monomer number concentration and mean particle size are shown in Fig. 3. The tungsten oxide particles decreased in size along the flame reactor due to solid evaporation. Approximately 4 cm from the burner inlet, all tungsten oxide particles were transformed into tungsten oxide vapors. Solid evaporation caused the monomer number concentration to increase. Tungsten oxide remained in the vapor phase until the temperature profile declined at approximately 10 cm in the flow direction. Saturation condition was promoted by cooling the flame reactor. Under supersaturation conditions, homogenous nucleation occurs to promote the emergence of new particles called clusters. Under this condition, the first nucleation occurs approximately 12 cm from the burner surface. Approximately 29 cm from the burner surface, most monomers had undergone nucleation. Nanoparticle growth that results in increased particle size occurred via coagulation and surface condensation.

Fig. 4a shows the evolution of the particle size distribution for synthesis condition (A), i.e., a methane flow rate of 1 L/min. From the burner surface, $x/L = 0$, along the length of the flame reactor to the end of the flame reactor at $x/L = 1.0$. x represents the distance from the burner surface, and L is the flame reactor length. Results of this calculation show that all initial polydispersed, submicrometer tungsten oxide particles evaporated and then reformed to generate nanoparticles. The number of particles decreased, while the mean size increased to 10.1, 16.2, and 19.1 nm at $x/L = 0.3$, 0.6, and 0.8, respectively, due to coagulation. The morphology of the generated particles obtained from the particle collector is shown in the FE-SEM image in the inset of Fig. 4a. At $x/L = 1.0$ from the burner surface, the geometric mean diameter was 21.5 nm with a geometric standard deviation of 1.5, and the particle size distribution is depicted in Fig. 4b. Agreement between the experimental and simulated results at the end of the reactor ($x/L = 1.0$) is also evident in the figure.

Changes in monomer number and mean particle size along the flame reactor under synthesis conditions (B), i.e., a methane flow rate of 0.8 L/min, are shown in Fig. 5. According to the simulated results, all particles were evaporated at a position 6 cm from the burner surface. The first clusters appeared approximately 8.5 cm

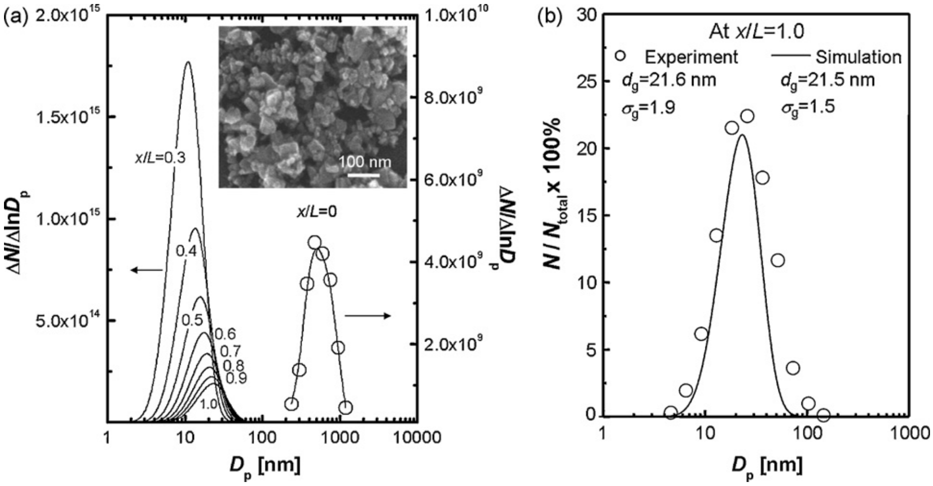

Fig. 4. (a) Evolution of the particle size distribution along the flame reactor from the tip of flame burner, $x/L = 0$ to the end of the flame reactor, $x/L = 1.0$ determined from the simulated results, and (b) comparison of the simulated and experimentally particle size distributions of the generated tungsten oxide particles. Inset: FE-SEM image of the generated tungsten oxide particles. Operating condition: methane (fuel) flow rate of 1 L/min and an oxygen (carrier gas) flow rate of 10 L/min.

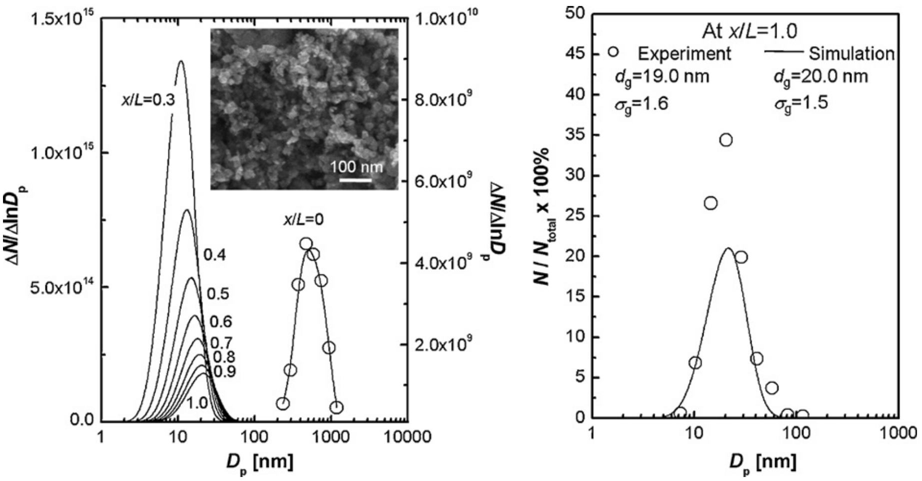

Fig. 6. (a) Evolution of the particle size distribution along the flame reactor from the tip of flame burner, $x/L = 0$ to the end of the flame reactor, $x/L = 1.0$ determined from the simulated results, and (b) comparison of the simulated and experimentally particle size distribution of the generated tungsten oxide particles. *Inset*: FE-SEM image of the generated tungsten oxide particles. Operating condition: methane (fuel) flow rate of 0.8 L/min and an oxygen (carrier gas) of 10 L/min.

from the burner surface. Most monomers were nucleated 23 cm from the burner surface. The evolution of the particle size distribution along the flame reactor under this condition is shown in Fig. 6a. Regeneration of particles from the vapor phase by nucleation, coagulation and surface condensation resulted in the particles growth, such that the particles were 10.2, 15.4, and 17.9 nm at $x/L = 0.3$, 0.6, and 0.8 cm from the burner surface. The inset of Fig. 6a shows the morphology of the generated particles obtained from the particle collector. Within the vicinity of the flame reactor ($x/L = 1.0$), the geometric mean diameter and standard deviation predicted by the simulation were 20.0 nm and 1.5, respectively. Comparison of the particle size distributions obtained from the simulated and experimental results revealed good agreement, as shown in Fig. 6b.

For a fuel flow rate of 0.5 L/min, i.e., synthesis condition (C), a bimodal size distribution was observed because supersaturation occurred prior to complete evaporation. The temperature distribution was too low to allow complete evaporation of the starting material. Agreement between the simulated and experimentally determined final particle size distribution is evident in Fig. 7. Submicrometer particles, which resulted from evaporation of the starting material, and nanoparticles were detected, as shown by the FE-SEM image in the inset of Fig. 7. Nanoparticles formed via regeneration of tungsten oxide monomers by nucleation, coagulation and surface condensation, whereas submicrometer size particles remained due to incomplete evaporation of the initial tungsten oxide particles. In addition, precursor having polydispersed particle size distribution, smaller particle size had higher evaporation rate than that of larger one resulting product with bimodal particle size distribution. For larger particle size, supersaturation had been reached before full evaporation occurred [4].

4.3. Effect of carrier gas flow rate

At a constant methane flow rate of 1 L/min, which was maintained by a carrier gas flow rate of 2 L/min (condition D), the simulation indicated that full evaporation of the feed material occurs more rapidly compared with a carrier gas flow rate of 10 L/min (condition A). Tungsten oxide was in the vapor phase approximately 2 cm from the burner surface because all feed material was evaporated, as shown in Fig. 8. The first cluster appeared approximately 10 cm from the burner surface due to supersaturation. Tungsten oxide vapor was not detected 21 cm from the burner surface. The evolution of the particle size distribution along the flame reactor using a carrier gas flow rate of 2 L/min and a fuel flow rate of 1 L/min (condition D) is summarized in Fig. 9a. The geometric mean diameters at $x/L = 0.3$, 0.6 and 0.8 were 24.2, 36.7, and 42.8 nm. The number concentration decreased with the length of flame reactor due to coagulation and surface condensation. The simulated

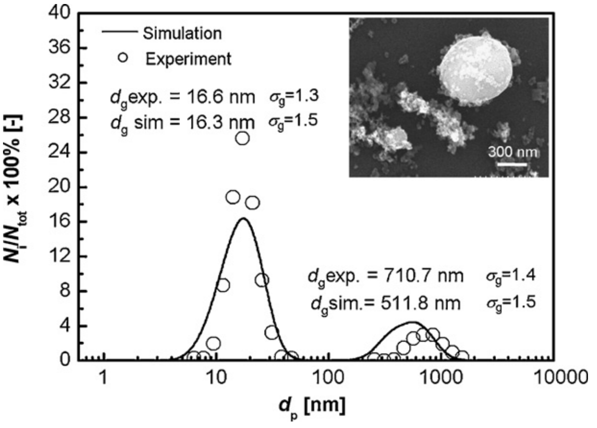

Fig. 7. Comparison of the simulated and experimentally particle size distribution of generated tungsten oxide particles. *Inset*: FE-SEM image of the generated tungsten oxide particles. Operating condition: methane (fuel) flow rate of 0.5 L/min and an oxygen (carrier gas) of 10 L/min.

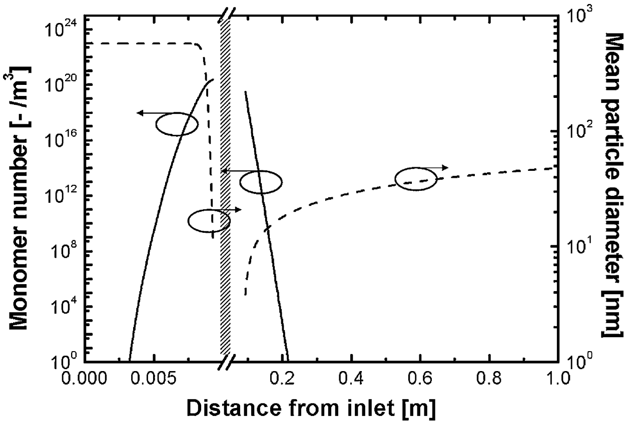

Fig. 8. Change in the monomer number concentration and average particle size along the furnace length. Operating condition: methane (fuel) flow rate of 1 L/min and an oxygen (carrier gas) of 2 L/min.

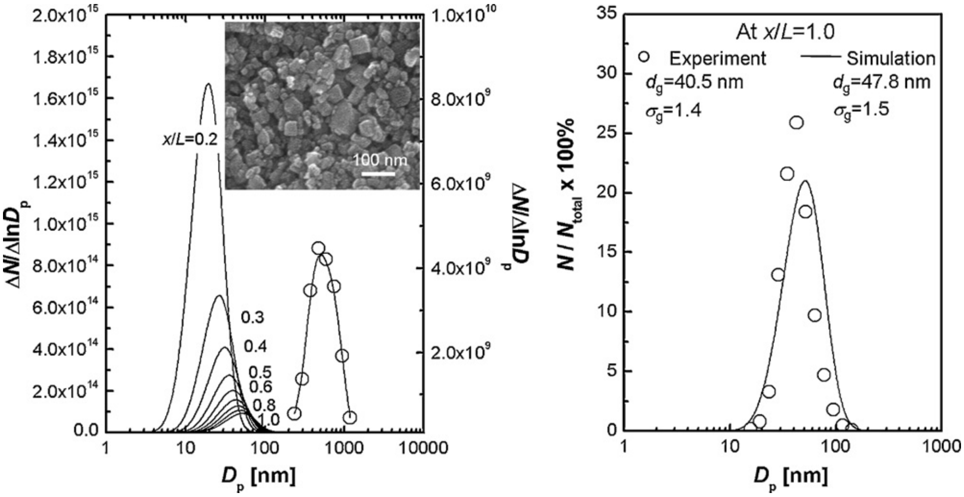

Fig. 9. (a) Evolution of the particle size distribution along the flame reactor from the tip of flame burner, $x/L = 0$ to the end of the flame reactor, $x/L = 1.0$ determined from the simulated results, and (b) comparison of the simulated and experimentally particle size distribution of the generated tungsten oxide particles. *Inset*: FE-SEM image of the generated tungsten oxide particles. Operating condition: methane (fuel) flow rate of 1 L/min and oxygen (carrier gas) flow rate of 2 L/min.

results were over-estimated by 15.3% compared with the experimental results, as shown in Fig. 9b. This result indicates that under these conditions, tungsten oxide undergoes grain growth and densification as shown in the FE-SEM image in the inset of Fig. 9a. Grain growth and densification were ignored in the simulation because of no sintering data of WO_3 particles was found. The grain growth and densification of particles can be obtained quantitatively such the quantitative measurement of particle aggregation and agglomeration by dynamic light scattering [23]. The limitation of the current research will become consideration in the future investigation.

5. Conclusions

Tungsten oxide nanoparticle formation using polydispersed and non-spherical submicrometer-micrometer sized in a solid-fed flame synthesis was studied numerically and the results were validated experimentally. From numerical results, it can be concluded that nanoparticles can be produced if evaporation of feed material is complete before the tungsten oxide vapor becomes supersaturated. This result was obtained using a methane flow rate of 0.8 or 1 L/min and a carrier gas flow rate of 10 L/min. For a methane flow rate of 0.5 L/min and a carrier gas flow rate of 10/min, a bimodal particle size distribution was obtained. When the methane flow rate was 1 L/min, decreasing the carrier gas flow rate to 2 L/min increased the size of generated particles because they had both a higher temperature distribution and a longer residence time. The simulation used in the present study gives a relatively accurate prediction of the final particles size distribution that results from fed-flame synthesis using a polydispersed and non-spherical starting material.

Acknowledgement

The Ministry of Education, Culture, Sports, Science and Technology (MEXT) of Japan (D.H.) is acknowledged for providing a doctoral scholarship.

References

[1] K. Okuyama, I.W. Lenggoro, Preparation of nanoparticles via spray route, Chem. Eng. Sci. 58 (2003) 537–547.
[2] A. Gutsch, H. Muhlenweg, M. Kramer, Tailor-made nanoparticles via gas-phase synthesis, Small 1 (2005) 30–46.
[3] S.E. Pratsinis, S.V.R. Mastrangelo, Material synthesis in aerosol reactors, Chem. Eng. Prog. 85 (1989) 62–66.
[4] W. Widiyastuti, A. Purwanto, W.N. Wang, F. Iskandar, H. Setyawan, K. Okuyama, Nanoparticle formation through solid-fed flame synthesis: experiment and modeling, AIChE J. 55 (2009) 885–895.
[5] D. Hidayat, A. Purwanto, W.N. Wang, K. Okuyama, Preparation of size-controlled tungsten oxide nanoparticles and evaluation of their adsorption performance, Mater. Res. Bull. 45 (2010) 165–173.
[6] C. Santato, M. Ulmann, J. Augustynski, Photoelectrochemical properties of nanostructured tungsten trioxide films, J. Phys. Chem. B 105 (2001) 936–940.
[7] J. Engweiler, J. Harf, A. Baiker, WO_x/TiO_2 catalysts prepared by grafting of tungsten alkoxides: morphological properties and catalytic behavior in the selective reduction of NO by NH_3, J. Catal. 159 (1996) 259–269.
[8] T. Siciliano, A. Tepore, G. Micocci, A. Serra, D. Manno, E. Filippo, WO_3 gas sensors prepared by thermal oxidization of tungsten, Sensor. Actuat. B Chem. 133 (2008) 321–326.
[9] C.G. Granqvist, Transparent conductors as solar energy materials: a panoramic review, Sol. Energ. Mater. Sol. C 91 (2007) 1529–1598.
[10] M.S. Wooldridge, Gas-phase combustion synthesis of particles, Prog. Energ. Combust. 24 (1998) 63–87.
[11] F. Gelbard, Y. Tambour, J.H. Seinfeld, Sectional representations for simulating aerosol dynamics, J. Colloid Interf. Sci. 76 (1980) 541–556.
[12] S.E. Pratsinis, Simultaneous nucleation, condensation, and coagulation in aerosol reactors, J. Colloid Interf. Sci. 124 (1988) 416–427.
[13] J.K. Jokiniemi, M. Lazaridis, K.E.J. Lehtinen, E.I. Kauppinen, Numerical-simulation of vapor aerosol dynamics in combustion processes, J. Aerosol Sci. 25 (1994) 429–446.
[14] K. Nakaso, T. Fujimoto, T. Seto, M. Shimada, K. Okuyama, M.M. Lunden, Size distribution change of titania nano-particle agglomerates generated by gas phase reaction, agglomeration, and sintering, Aerosol Sci. Technol. 35 (2001) 929–947.
[15] A. Prakash, A.P. Bapat, M.R. Zachariah, A simple numerical algorithm and software for solution of nucleation, surface growth, and coagulation problems, Aerosol Sci. Technol. 37 (2003) 892–898.
[16] C.J. Geankoplis, Transport Processes and Separation Process Principles (Includes Unit Operation), Fourth ed., Pearson Education, Inc., New York, 2003.
[17] U. Ulusoy, Application of ANOVA to image analysis results of talc particles produced by different milling, Powder Technol. 188 (2008) 133–138.
[18] W. Widiyastuti, W.N. Wang, I.W. Lenggoro, F. Iskandar, K. Okuyama, Simulation and experimental study of spray pyrolysis of polydispersed droplets, J. Mater. Res. 22 (2007) 1888–1898.
[19] M.M.R. Williams, S.K. Loyalka, Aerosol Science Theory and Practice: With Special Applications to the Nuclear Industry, first edition, Pergamon Press, Oxford, 1991.
[20] W.H. Kohl, Handbook of Materials and Techniques Vacuum Devices, AIP Press, New York, 1967.
[21] C. Vladuta, L. Amdronic, M. Visa, A. Duta, Ceramic interface properties evaluation based on contact angle measurement, Surf. Coat. Technol. 202 (2008) 2448–2452.
[22] B.E. Poling, J.M. Prausnitz, J.P. O'Connell, The Properties of Gases and Liquids, The McGraw-Hill Companies, Inc., New York, 2001.
[23] A. Teleki, R. Wengeler, L. Wengeler, H. Nirschl, S.E. Pratsinis, Distinguishing between aggregates and agglomerates of flame-made TiO_2 by high-pressure dispersion, Powder Technol. 181 (2008) 292–300.